Simulation, experiment, and performance of a 4 MV induction voltage adder machine for flash x-ray radiography

Hao Wei, Jiahui Yin, Pengfei Zhang, Fengju Sun, Aici Qiu, Tianxue Liang, Xiaofeng Jiang, Zhiguo Wang, Jiang Sun, Qiangfeng Luo, Hailiang Yang, Weibo Yao, Hongyu Jiang, and Hanyu Wu

State Key Laboratory of Intense Pulsed Radiation Simulation and Effect, Northwest Institute of Nuclear Technology, Xi'an 710049, China

(Received 23 September 2020; accepted 21 January 2021; published 23 February 2021)

A 4 MV flash x-ray radiographic machine based on induction voltage adders has been developed. The configuration and design of this machine are reviewed. A three-dimensional, fully electromagnetic model and a circuit simulation model are established to compare with the experiments. The simulation results are in overall agreement with the electrical measurements. The pulsed power performances and output fluctuations of this machine over successive shot sequences are demonstrated. Among the 54 shots, the average peak output voltage is 4.4 ± 0.3 MV (1-σ) and the average diode current is 81.6 ± 4.5 kA (1-σ). Four typical malfunction modes are identified shot by shot including the diode-impedance collapse, insulator flashover, core saturation, and drive mistiming. Some remarkable features from each fault mode are recognized. The first-to-last time spreads of the four drive pluses, t_{spread}, are chosen to quantify the drive synchronization and the influences of the t_{spread} on the peak voltages and diode currents are summarized from the almost 100 shots since the machine was commissioned. It is found that, in order to achieve a voltage of up to 4 MV, t_{spread} should not exceed 25 ns, which is approximately twice the time for electromagnetic wave propagation from the first cavity to the last cavity in vacuum. In addition, the rise time and FWHM duration of output voltages varying with t_{spread} are given. The results indicate that the rise time changes little at the beginning but increases exponentially once the t_{spread} exceeds 30 ns. The FWHM duration nearly increases linearly with t_{spread}.

DOI: 10.1103/PhysRevAccelBeams.24.020402

I. INTRODUCTION

Flash radiography using high-brightness, small focal spot x rays generated from pulsed-power-accelerator-driven electron-beam diodes plays an important role in hydrodynamic experiments [1–6]. Presently, there are two main approaches to produce high-brightness x rays, which are based on the technologies of linear induction accelerators (LIAs) and induction voltage adders (IVAs) [7–10]. IVA-type radiographic sources are more compact and less expensive than LIAs [11–13]. They avoid long-distance transport and beam breakup instability (BBU) of intense electron beams [14,15]. Several IVA-type radiographic machines have been developed across the world, including the dual beam radiographic facility Cygnus [16,17], the Radiographic Integrated Test Stand (RITS) in the U.S. [18,19], the 14 MV Merlin accelerator under construction in the U.K. [20,21], and a 4 MV x-ray machine being manufactured at China Academy of Engineering Physics (CAEP) [22,23].

Differing from the x-ray machine developed by the CAEP using six independent Tesla generators producing prime pulses to drive a IVA with six-stage induction cavites assembled in series, a 4 MV flash x-ray radiographic source named Jianguang-II was developed at the Northwest Institute of Nuclear Technology in China during 2018. The design details and initial experimental results were presented in Ref. [24]. The current paper emphasizes detailed comparisons between the electromagnetic (EM) models, circuit simulations, and experimental results. Moreover, special attention is paid to machine reliability and output fluctuations. Pulsed-power performances are illustrated over successive shot sequences, which includes both the normal operation and aborted shots. Several typical malfunction modes and their effects on the output parameters are analyzed.

This paper is organized as follows. A brief introduction of the design of this 4 MV IVA machine is given in Sec. II. Section III presents direct comparisons between the EM models, circuit simulations, and the electrical measurements from shot 19-007. A time-varying load model is utilized in the circuit simulation to eliminate the pulse front discrepancies between the EM models and measurements. In Sec. IV, the machine performances and output fluctuations including peak output voltages, diode currents, x-ray durations, and radiated doses are demonstrated in detail over 54 successive shots. Typical machine malfunctions are described in Sec. V. Several failure modes including the diode-impedance collapse, insulator-stack flashover, core saturation, and drive mistiming are analyzed shot by shot. In Sec. VI, the influences of drive jitters of the four driving pulses on the output parameters are presented. The work is summarized in Sec. VII.

II. EXPERIMENTAL SETUP OF THE 4 MV IVA MACHINE

As shown in Fig. 1, the positive-polarity 4 MV machine comprised three subsystems: a prime pulsed-power source, an induction voltage adder, and an x-ray electron-beam diode. The prime pulsed-power source consisted of two Marx generators and four 6 Ω deionized water coaxial pulse lines. Unlike in other IVA machines [25–28], only two-stage pulse compressions were employed in this machine. Each low-inductance, fast Marx generator charged two pulse-forming lines (PFLs) to approximately 2.2 MV in less than 370 ns [24]. Four electrically triggered, SF_6-insulated gas switches were chosen to transfer energy from the PFLs to the output lines [29]. Subsequently, a self-breaking water switch was used to further sharpen the rise time. Ultimately, four forward-going pulses with peak voltages of up to 1 MV and rise time of 15 ns could be reliably generated into a 6 Ω matched load. The IVA consisted of four induction cavities connected in series, each of which was single-point driven by a coaxial water line. As illustrated in Fig. 1(b), a stepped inner stalk was inserted into the cavities to form a vacuum transmission line with the cavity bores. The vacuum-insulated transmission operated with the cathode electric field below the emission threshold, whose impedances increased from 30 Ω in the first cavity to 120 Ω in the last.

The rod-pinch diode (RPD) was chosen to create bremsstrahlung x rays, which was believed to be optimal at voltage levels of approximately 4 MV [30–33]. The RPD structure was illustrated in Fig. 2. The cathode disk was made of 4-mm-thick graphite, and the diameter of the center hole was 20 mm. A tungsten needle served as the anode, which extended past approximately 17 mm beyond the cathode disk. During the dozens of shots in this paper, the diameters of the tungsten needles were either 1.6 or 2.0 mm, depending on the compromise between the dose and the focal spot size.

In order to monitor the voltage addition and transmission process, four capacitive voltage dividers were installed on the outer cylinder downstream of each cavity, which was labeled from V_1 to V_4 respectively. In addition, there were

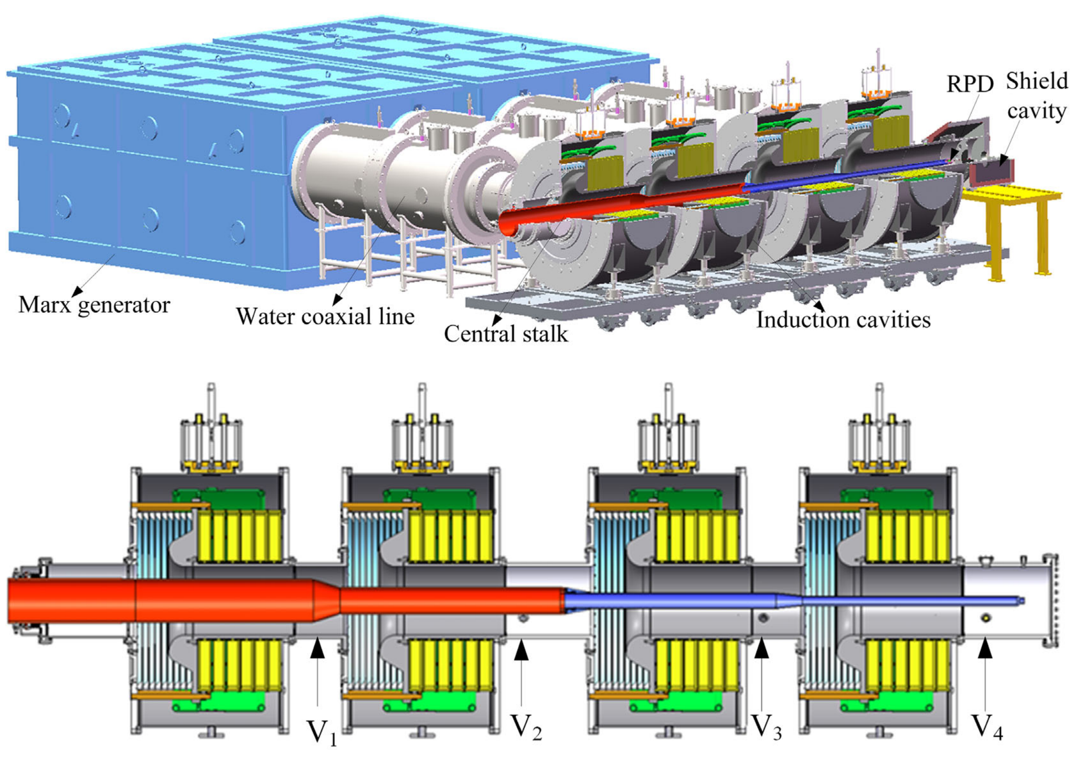

FIG. 1. (a) Overview of the 4 MV IVA-type flash x-ray radiographic machine named Jianguang-II and (b) the cross section to illustrate the four-stage induction cavities and the central stalk. Four capacitive voltage dividers were installed downstream of each cavity, which was labeled from V_1 to V_4. This facility has a volume of 6 m × 9 m × 2.5 m.

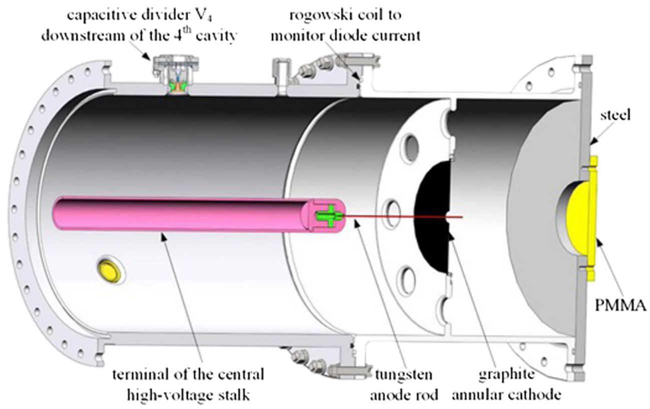

FIG. 2. The structure of the rod-pinch diode (RPD) used to produce high-brightness x rays.

three rogowski coils along the current loop, two of which were located downstream of the second and last cavity, and the another one was located nearby the diode to measure the diode current. All the probe locations were marked in Figs. 1(b) and 2.

The diode voltage, V_{diode}, was achieved by an inductive correction from the measured voltage downstream of the last cavity, V_4, which could be expressed as

$$V_{\mathrm{diode}} = V_4 - L_0 \frac{dI_{\mathrm{diode}}}{dt}, \tag{1}$$

where I_{diode} is the diode current, and the L_0 is the vacuum inductance between the V_4 probe location and the diode gap, which is estimated to be approximately 360 nH for the RPD structure shown in Fig. 2.

The dynamic impedance of RPD is defined by

$$Z_{\mathrm{diode}}(t) = \frac{V_{\mathrm{diode}}}{I_{\mathrm{diode}}}. \tag{2}$$

III. 3D EM MODELS AND CIRCUIT SIMULATIONS

Three-dimensional, fully electromagnetic models are essential tools in the design and analysis of pulsed-power systems [34–37]. In order to better understand the voltage addition process and verify the electrical measurements, a 3D EM model of the four-stage IVA was established under the Cartesian coordinate. To accurately model the realistic voltage reflections at the cavity inlet ports, a one-meter-length coaxial water line was connected to each cavity. Each water line was driven by a voltage source, whose driving impedance was equal to be 6 Ω. The incident voltage was illustrated in Fig. 3, where it peaked at approximately 750 kV with two Marx generators charged at ±50 kV dc. The single-cavity 3D model in Ref. [38] was modified to model the four-cavity IVA. At the IVA output end, a constant resistive load of 50 Ω was used to represent the steady impedance of rod-pinch diodes. In addition, a circuit model of the four-stage IVA was also established. It differed from the 3D EM model in that it used a time-varying load impedance shown in Fig. 4. The dynamic impedance was obtained from shot 19-007 according to the Eqs. (1) and (2), which can be fitted by a fifth-order polynomial.

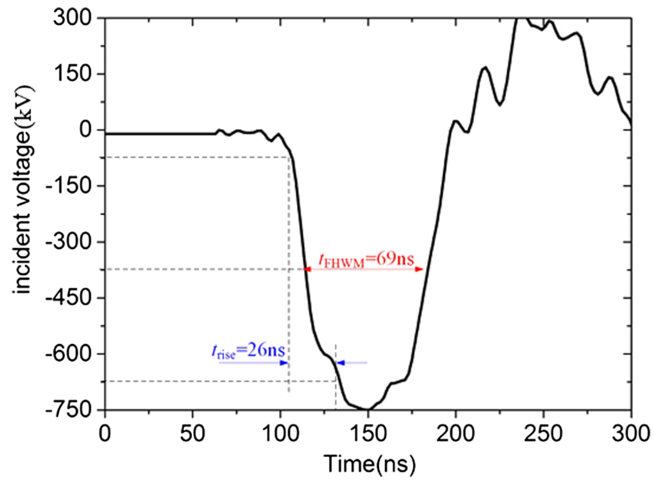

FIG. 3. Incident voltage used in the 3D EM model and circuit simulation. This is the measured load voltage when each pulse line is terminated with a matched load of approximately 6 Ω.

In Fig. 5, the simulated voltage waveforms downstream of each cavity from the 3D EM model and circuit simulation are compared with the typical shot 19-007. Both the EM and circuit simulation results are generally consistent with the measurements from the first through the third cavity. Downstream of the last cavity, the discrepancy at the pulse front between the EM model and measurement might be resulted from the assumption of the constant-impedance diode. The electric field distribution through the central plane at the peak voltage time is illustrated in Fig. 6.

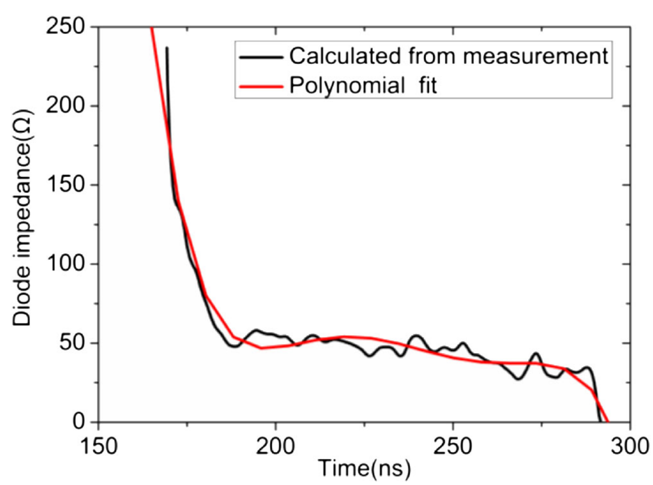

FIG. 4. Diode impedance trace used in the circuit simulation. The black line is the calculated impedance from electrical measurements of shot 19-007 according to Eqs. (1) and (2), and the red line is a fifth-order polynomial fit curve used in the circuit.

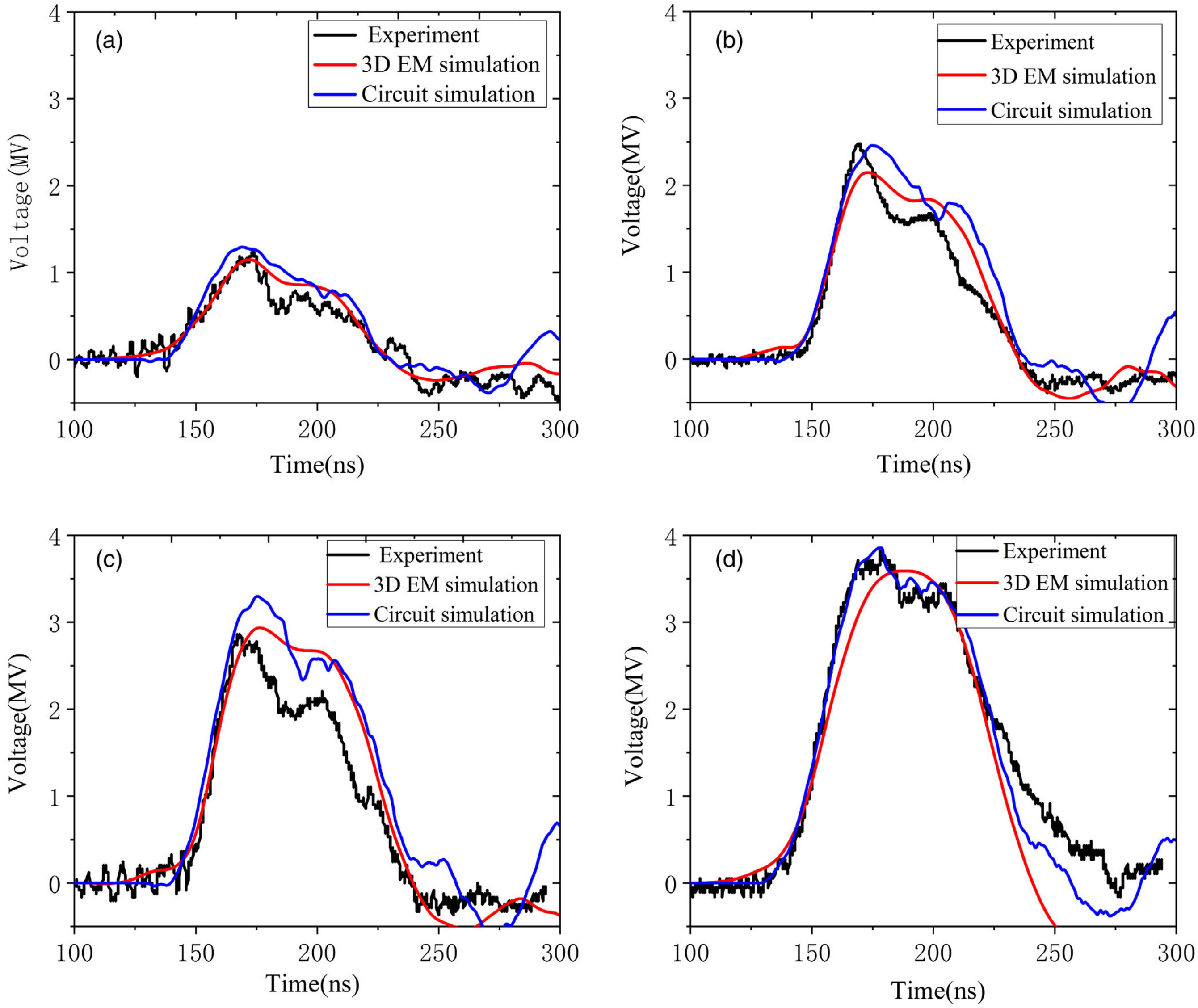

FIG. 5. Comparisons of 3D EM (red curves), circuit simulation (blue curves), and shot 19-007 (black curves). The voltages were monitored downstream of each cavity labeled in Fig. 1(b). The two Marx generators were charged to ±50 kV.

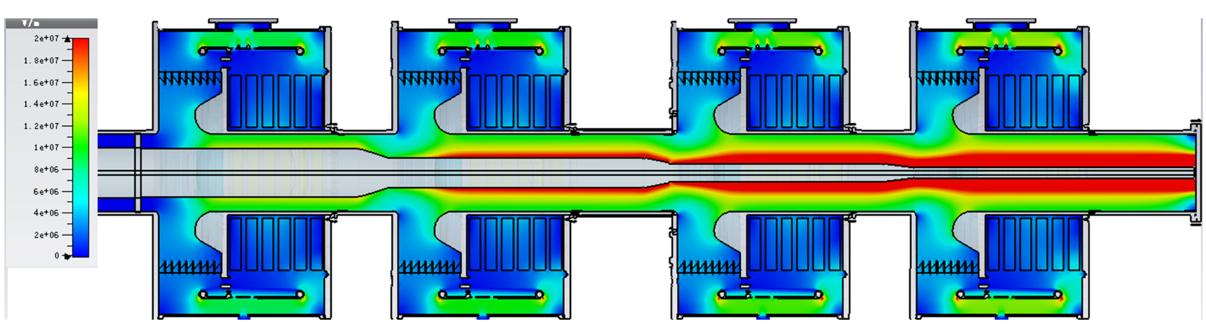

FIG. 6. Electric field distribution through the central plane of the four-stage IVA at the peak voltage time.

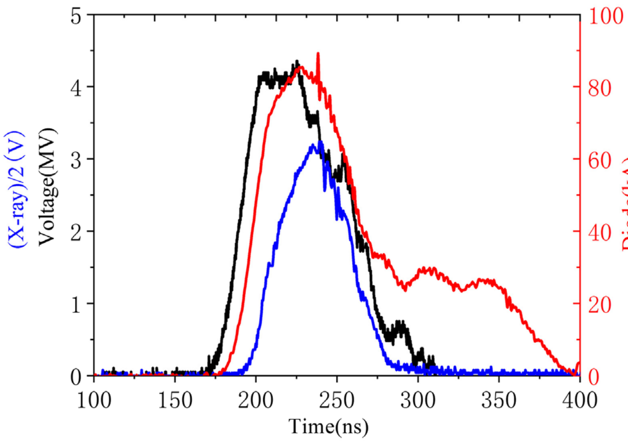

FIG. 7. Typical output voltage (black), diode current (red), and x-ray signals (blue) from shot 19-054. The Marx generators were charged to ±60 kV for this shot.

IV. MACHINE PERFORMANCE

A. Typical output characteristics

Typically, the IVA machine was operated with the Marx generators charged to ±60 kV. In order to avoid the unnecessary disturbance that might be resulted from the unwanted malfunctions such as the insulator flashover, several limited shots were conducted with the Marx charge voltage decreased to ±50 kV, to validate and verify the simulation model and probe sensitivity. The output voltage, diode current, and x-ray signal under a typical ±60 kV charge shot are illustrated in Fig. 7. The peak output voltage is 4.2 MV with a rise time of 21 ns and a full width at half maximum (FWHM) time of 70 ns. This V_4 voltage divider is located approximately 0.4 m upstream of the diode. Therefore, the actual diode voltage should be corrected by Eq. (1). This method has been widely used in the case that the measurement probes cannot be accessed directly or conveniently [39,40]. The peak diode current is approximately

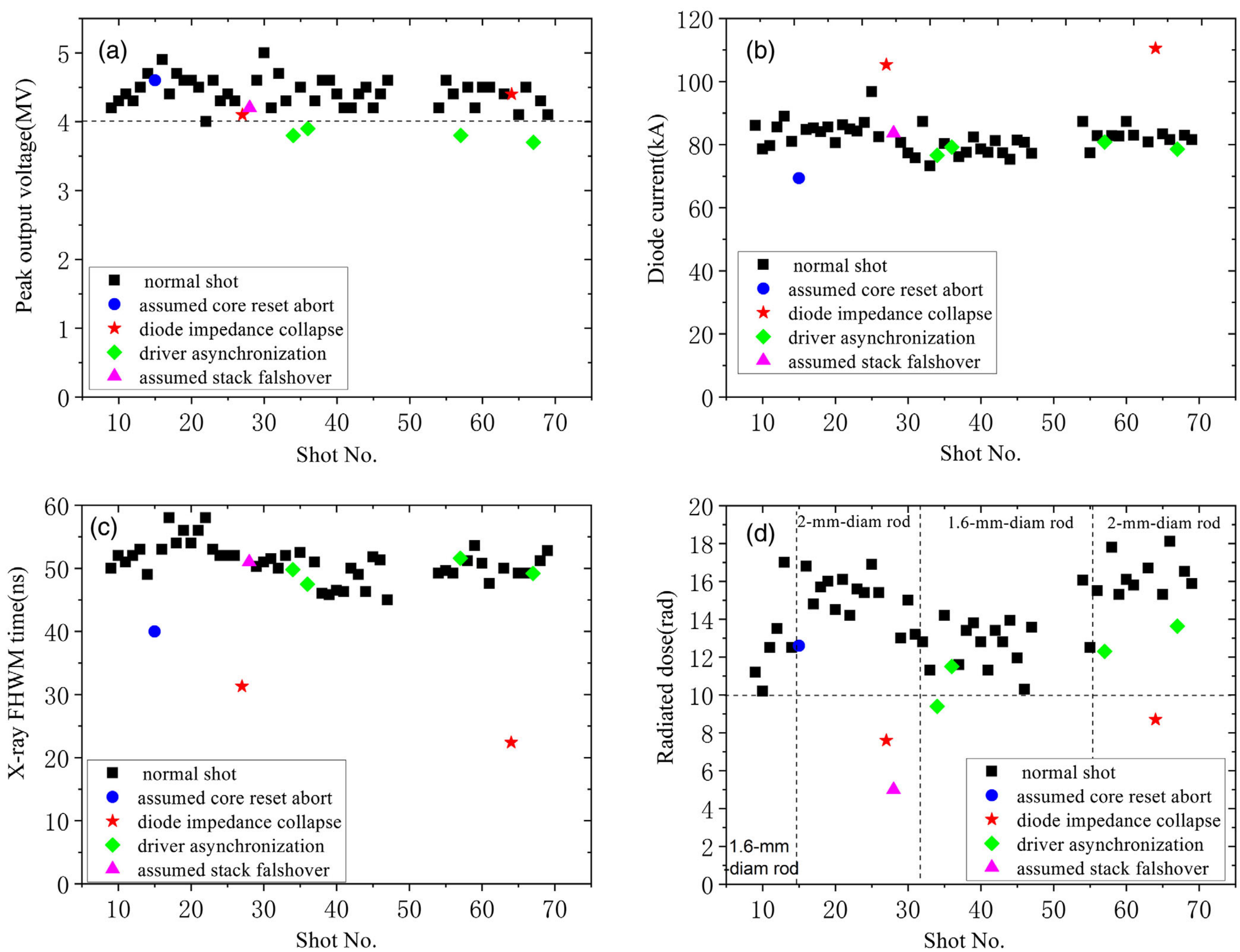

FIG. 8. Output fluctuation of the 4 MV IVA machine over 54 successive shots at ±60 kV. (a) Peak output voltage, (b) peak diode current, (c) radiated dose, and (d) x-ray duration time. The normal shots are marked with black squares, and each malfunction mode is marked with a particular color and symbol.

TABLE I. Comparison of 4 MV IVA output parameters of good and poor shots. The time spreads in the second column indicate the first-to-last spread of four drive pulses and represent drive synchronization.

Shot number	Time spread/ns	Peak voltage/MV	Voltage FWHM/ns	Diode current/kA	X-ray FWHM/ns	Dose@1 m/Rad	Malfunction
19-054	11.9	4.2	70	87.3	49	16.0	Normal shot
19-027	21.7	4.1	49	105.3	31	7.6	Impedance collapse
19-064	12.0	4.4	37	110.5	22	8.7	
19-028	14.8	4.2	38	83.6	51	5.0	Stack flashover
19-015	8.80	4.6	57	69.4	40	12.6	Core saturation
19-034	37.6	3.8	71	76.6	50	9.4	Drive mistiming

87 kA. The FWHM time of x rays is approximately 49 ns measured by a Compton detector. The measured radiated dose is approximately 16 rad [lithium fluoride (LiF)] at one-meter forward by a thermoluminescent dosimeter.

B. Output fluctuations over 54 successive shots

The shot reproducibility of this 4 MV IVA machine was examined. Fluctuations in pulsed power performance, including output variations in the peak output voltage, diode current, radiated dose, and x-ray duration time over successive shot sequences are shown in Fig. 8. Fifty-four shots conducted at ± 60 kV are included in these statistics. The six shots labeled from shot 048 to shot 053 were excluded due to operation at ± 50 kV.

Figure 8(a) presents the peak output voltages over the 54 successive shots. The average peak output voltage is 4.4 ± 0.3 MV (1-σ). Most shots peak above the anticipated 4 MV except for shots 034, 036, 057, and 067. Those lower peaks are more likely related to the asynchronous drive of feed pulses. This will be discussed further in Sec. VI.

Figure 8(b) shows the variations in the peak diode current during the tests. There are two types of abnormal shots. During shots 027 and 064, the diode current increases sharply to more than 100 kA. Combined with the x-ray duration time illustrated in Fig. 8(c), it is indicated that the abnormality is probably attributed to a catastrophic diode-impedance collapse. For the abnormal shot 015, the diode current decreases to approximately 70 kA and the x-ray duration decreases to 40 ns. The reason for this is not clear. However, the distinct increase in the core leakage current suggests that it might be due to a failed core reset, which will be further discussed in Sec. VI. The average diode current is 81.6 ± 4.5 kA (1-σ) except for the three poor shots mentioned above.

Figure 8(c) shows how the x-ray duration time fluctuates in this series. Excluding the abrupt decreases noted among the three shots associated with abnormal diode currents, the average x-ray duration time is 51.0 ± 2.8 ns (1-σ).

Figure 8(d) shows how the radiated dose varies. Only four shot's doses are less than 10.0 rad (LiF). The sharp decreases in doses of shots 027 and 064 are caused by diode-impedance collapse. The slight dose decrease of shot 034 might be correlated to asynchronous drive of the four feed pulses. It is still difficult to identify the reason for the considerable dose decrease of shot 028. It is speculated to be resulted from the insulator-stack flashover in the cavities. Notably, some radiated dose fluctuations in Fig. 8(d) originate from the variations of diode geometry parameters such as the anode-rod diameter. This has been experimentally verified by extensive RPD operation at 2 to 6 MV on the Asterix generator [32,41].

Detailed comparisons of the IVA output parameters produced by these four typical malfunctions with the normal shots are given in Table I. The most common consequence of the failure is a large decrease in radiated doses, especially when the diode-impedance collapse or the insulator-stack-flashover occurs.

V. ABORTED SHOTS AND MACHINE MALFUNCTIONS

In this section, the typical poor shots and their effects on the output parameters and critical components are discussed shot by shot. The normal shot 19-054 is chosen as a reference and compared with the poor shots.

A. Diode-impedance collapse

Electrical measurements from a diode-impedance collapse shot and the normal shot 054 are compared in Fig. 9. The temporary impedance history in Fig. 9(d) indicates that the diode impedance of shot 064 does collapse much earlier than the normal shot. The most remarkable feature in this case is the sharp increase at the flattop of the diode currents. As a result, the output voltage and x-ray waveform was chopped down immediately. The x-ray duration time and radiated dose decrease to nearly half that of a normal shot. The sharp increase in the diode current waveform occurs only under this malfunction, which has become a criterion to determine whether the diode-impedance collapse occurred. Similar current waveform features have been observed during the impedance collapse of self-magnetic-pinch diodes on the RITS-6 machine [42,43]. For the 4 MV IVA machine herein, the external factor contributing most to the impedance collapse is the continual swinging of the anode needles, which is caused by the vacuum pump in the diode region [43]. The probability of diode-impedance

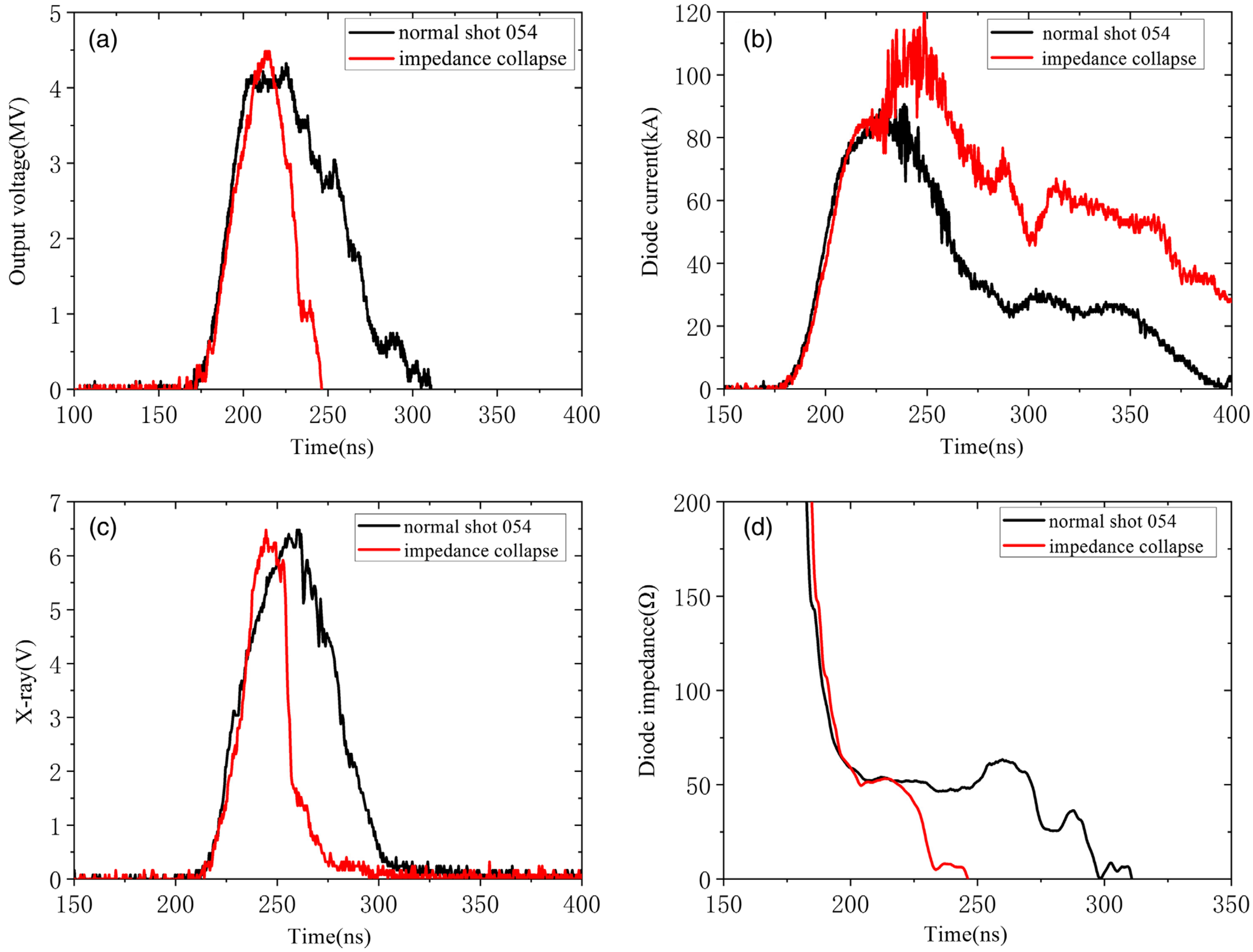

FIG. 9. Comparison of electrical measurements from the impedance-collapse shot 064 (red traces) and the normal shot 054 (black traces). (a) Output voltage, (b) diode current, (c) Compton detected x ray, and (d) calculated diode impedance profiles according to Eqs. (1) and (2).

collapse failure is approximately 4% (two occurrences over the 54 shots).

B. Insulator-stack flashover

Figure 10 provides the comparisons of the aborted shot 028 and the normal shot 054. As similar in Fig. 9(a), the output voltage is shortened at the pulse flattop. However, unlike the diode-impedance collapse example shown in Fig. 9(b), the diode current has a much lower peak and more oscillations. It is odd that the radiated dose decreases to a low value whereas the x-ray duration changes little. Additional information is required to understand what occurs. As shown in Fig. 10(d), the measured voltage downstream of the third cavity is almost identical to that of the normal shot. It is indicated that the fault is more likely to appear in the last cavity. The discrepancy between the posterior waveforms of the feed currents of the fourth cavity suggests that the insulator-stack flashover does occur within the last cavity. Recent machine maintenance validated this speculation. Three insulator rings within the fourth cavity are mechanically broken, and then some bulk breakdown occurs along the noted cracks. The abnormal waveforms disappear after the insulator stack is replaced.

In fact, calculated from the Martin's well-known vacuum flash equation, the failure probability of a nine-stage insulator stack with a total length of 310 mm should be quite low for our conservative design [44–46]. Observation of insulator surface traces suggested that nearly all of the flashover occur underneath several insulator pieces that were just exposed under the radial feed gap. In addition, all the flash originated from the anodes and expanded towards the cathodes. It was thought that the insulator-stack flash were mainly resulted from the poor operating environment. Abundant diode debris were created and dropped into the lacunas near the anode triple junction region at the bottom

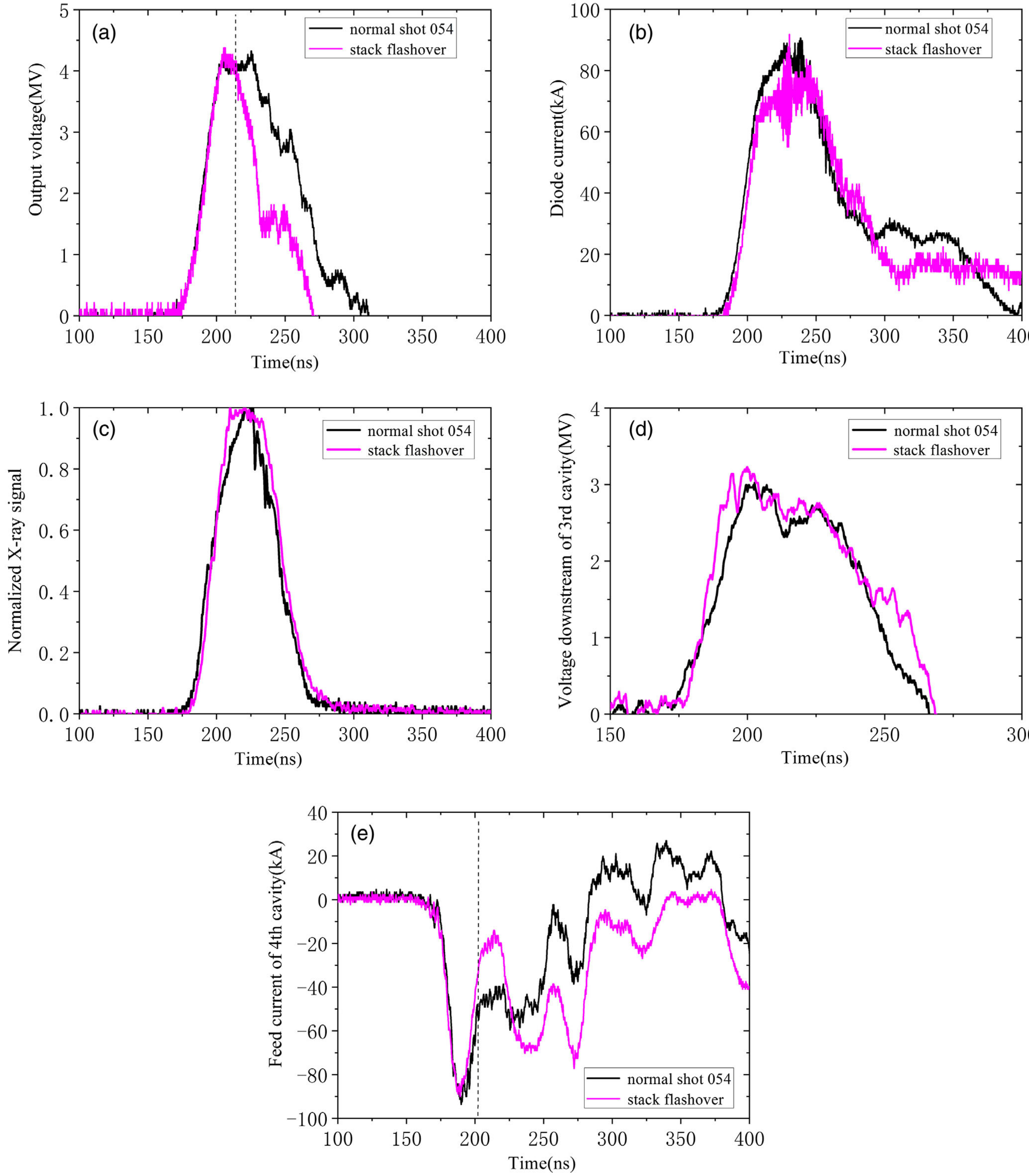

FIG. 10. Comparison of electrical measurements between the insulator-stack-flashover shot 028 (fuchsia traces) and the normal shot 054 (black traces). (a) Output voltage, (b) diode current, (c) normalized x-ray signals, (d) voltage downstream of the third cavity, and (e) feed current of the fourth cavity.

of the insulator stack. These tiny debris were not cleaned timely. Generally, a clear up maintenance was performed only after every five or even more shots.

C. Core saturation

Electrical signals from the aborted shot 015 and the normal shot 054 are compared in Fig. 11. The peak output

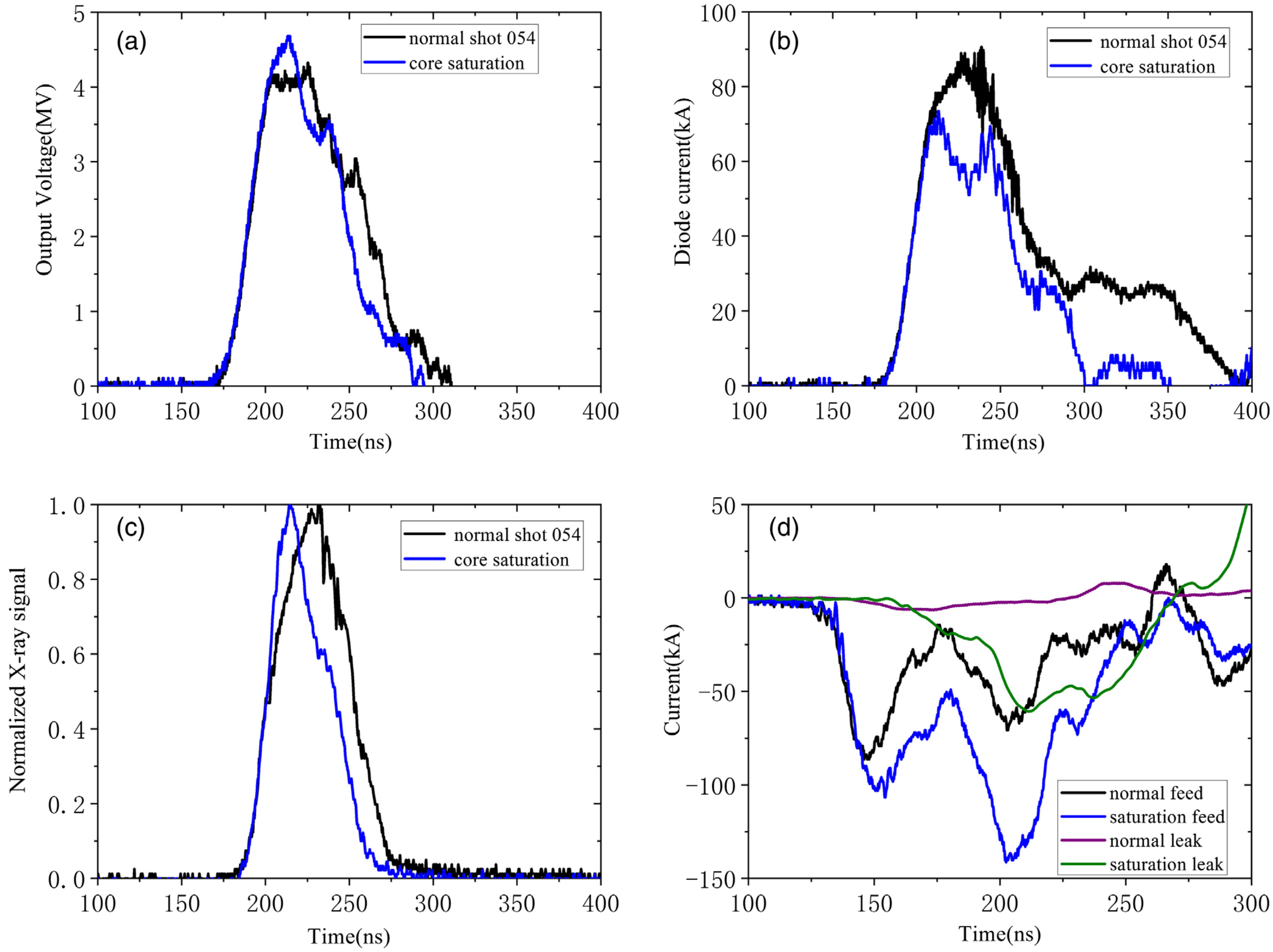

FIG. 11. Comparison of electrical measurements from the core-saturation shot 015 (blue traces) and the normal shot 054 (black traces). (a) Output voltage, (b) diode current, (c) normalized x-ray signals, and (d) feed and leakage currents from the second cavity. The latter indicates that the cores are saturated.

voltage increases from 4.2 to 4.6 MV but the FWHM time decreases from 70 to 57 ns, and the diode current also decreases from 87 to 69 kA. Consequently, the x-ray duration time and the radiated dose decreases more or less. Just from Fig. 11(a) to Fig. 11(c), it is no way to determine what failure mode occurs. An insulator-stack flashover might also bring the above waveform features. Figure 11(d) shows the cavity feed current and the leakage current flowing around Metglas cores. For the normal shot, the core leakage current is less than 6 kA, i.e., approximately 7% of the feed current. However, for shot 015, the leakage current starts low and then increases to approximately 60 kA. The cavity feed current further increases to approximately twice that of the first peak. This phenomenon is quite consistent with the core saturation [47–49]. The core-saturation malfunction is probably due to the incorrect operation of the premagnetized subsystem. It occurs rarely and has been noted only once since the machine was commissioned.

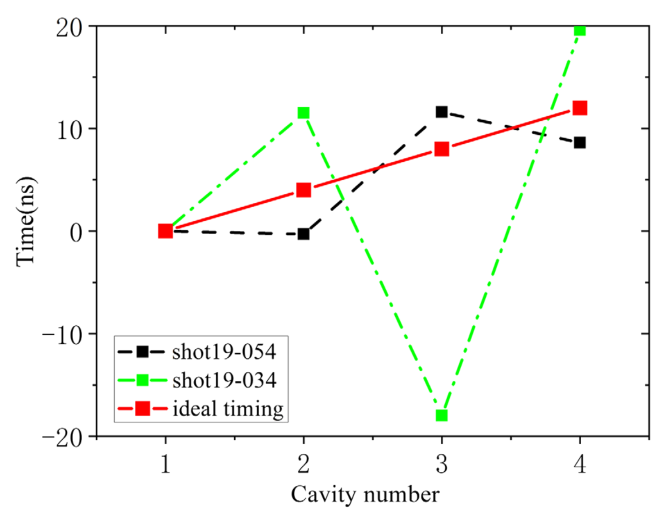

FIG. 12. Relative drive timing of the four-cavity IVA for shot 054 (black trace) and shot 034 (green trace). The ideal timing (red traces) is also shown.

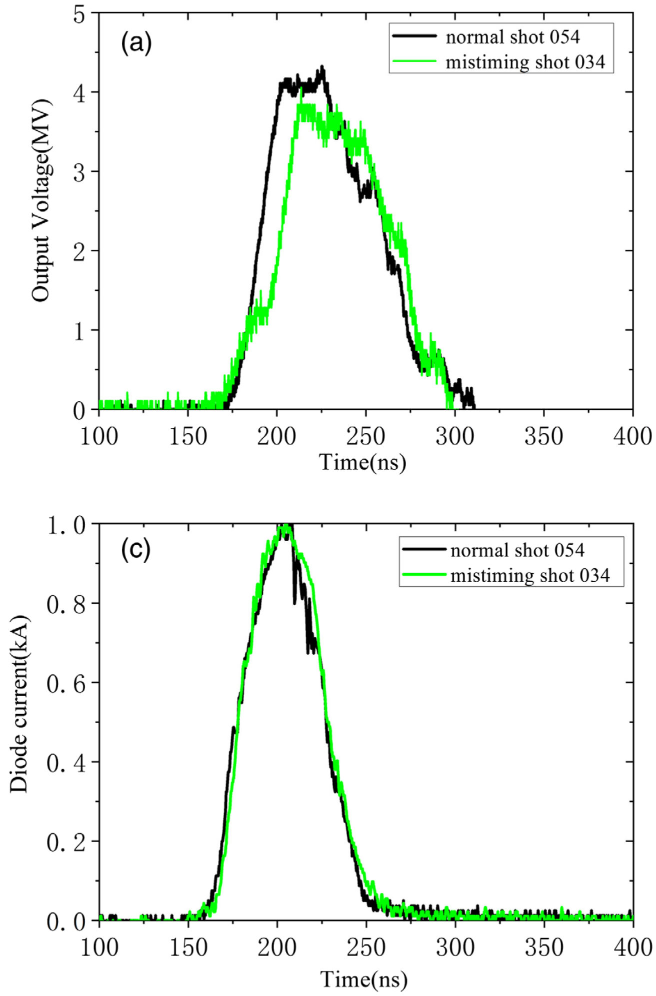

FIG. 13. Comparisons of electrical measurements from the mistiming shot 034 (green trace) and the normal shot 054 (black traces). (a) Output voltage, (b) diode current, (c) normalized x-ray signals, and (d) calculated diode impedance.

D. Asynchronous drive

Time jitters among the driving pulses is essential to the reliability and stability of this IVA machine [10,28,50–52]. Because the four driving pulses come from two Marx generators and are transferred via four separate electrically triggered gas switches, the arrival times are inevitably nonideal. In this paper, the first-to-last time spread between the four drive pulses, t_{spread}, is chosen to quantify the drive synchronization. Alternatively, the root-mean-square (rms) error of deviations between the actual and ideal timing can also be preferred to quantify drive synchronization.

Figure 12 shows the relative drive timing between the normal shot 054 and the mistimed shot 034. The first cavity arrival time is chosen as a datum time, and the arrival times of other cavities are shifted. In the ideal timing, t_{spread} is equal to 12 ns, which accords to the cavity spacing of this 4 MV IVA machine. The t_{spread} of shot 034 increases to 38 ns, which badly deviates from the ideal value of 12.0 ns. During the normal shot 054, although the drive timing also

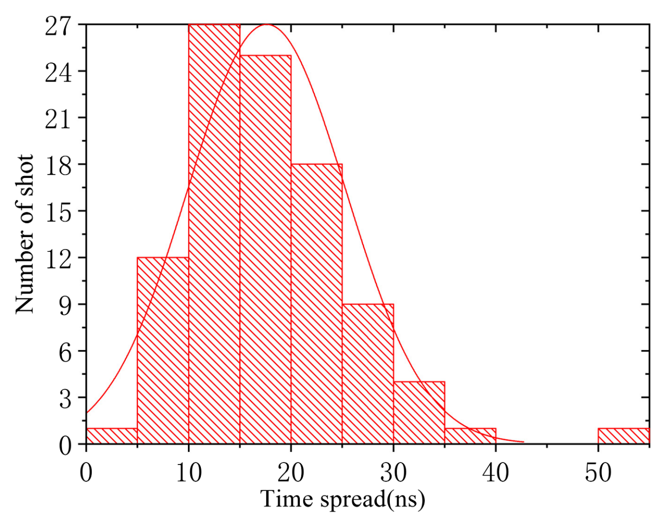

FIG. 14. Histogram of the first-to-last time spread for four drive pulses over a 98 shot sequence.

departs from the ideal one, t_{spread} matches that of the ideal timing.

Figure 13 compares electrical signals from the mistiming shot 034 and the normal shot 054. A remarkable feature of the mistiming case is the prolonged pulse rise time. The output voltage rise time (0.1–0.9) increases from 21 to 41 ns, while the peak voltage decreases from 4.2 to 3.8 MV. Surprisingly, the x-ray duration and the diode impedance trace changes little, which is illustrated in the Figs. 13(c) and 13(d). It seems that the decrease in dV/dt does not degrade the diode impedance characteristics substantially as previously expected. In fact, what extent of dV/dt can be accepted or tolerated is of great significance to the design of flash x-ray machines. Generally, to achieve good electron-beam diode reliability and reproducibility, the allowable maximum rise time must decrease as the diode voltage increases.

VI. INFLUENCE OF DRIVE JITTER

The effects of drive jitters on the operation and output parameters of IVA and linear transformer drivers (LTD) have been investigated widely by means of circuit simulations [10,18,50,52,53], whereas the results usually lack adequate experimental validations. In this section, the influences of drive jitters on the IVA pulsed power performances are presented from almost a hundred experimental shots. The histogram of the first-to-last time spread among the four drive pulses, t_{spread}, is shown in Fig. 14. The

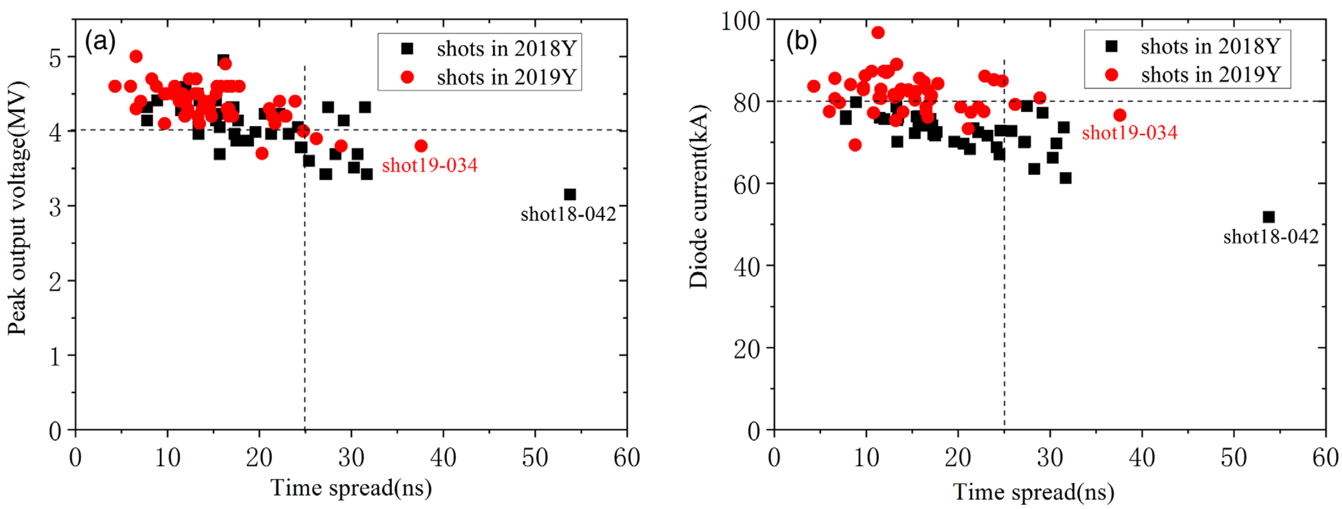

FIG. 15. Effects of the first-to-last time spread (t_{spread}) on the peak output voltages and diode currents in a statistics of almost 100 shots. (a) Peak output voltage, and (b) peak diode current. The black dots represent the shots conducted in 2018, while the red dot represent the shots in 2019 after a maintenance on the four electrically-triggered gas switches to improve the drive synchronous.

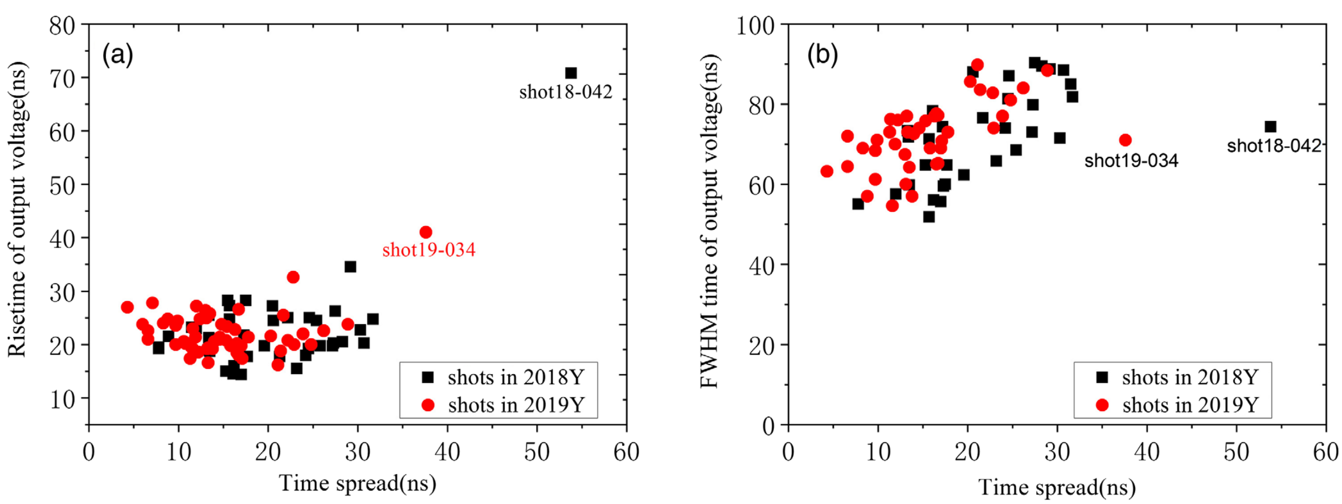

FIG. 16. Effects of the first-to-last time spread (t_{spread}) on the rise time and FWHM time of output voltages in a statistics of almost 100 shots. (a) rise time, and (b) FWHM time. The black dots represent the shots conducted in 2018, while the red dots represent the shots in 2019 after a maintenance on the four electrically triggered gas switches to improve the drive synchronous.

t_{spread} approximates to be a normal distribution in statistics, with a mean of 17.6 ns and a standard deviation of 7.7 ns. The probabilities of encountering a t_{spread} of less than 25 and 30 ns are about 83% and 95%, respectively.

Figure 15 illustrates how the peak output voltage and diode current vary with t_{spread}. The diode-impedance collapse shots were excluded. Shots conducted during 2018 and 2019 are marked with different colors and symbols. After a maintenance of the four electrically triggered gas switches during early 2019, the deviation in t_{spread} becomes smaller, and higher voltages and diode currents are acquired. Both the peak output voltage and diode current gradually decrease as t_{spread} increases. Even when t_{spread} is constant, there exist various combinations of arrival timing. Hence, the output parameters are distributed in a broad range. To achieve a voltage of 4 MV, t_{spread} should not exceed 25 ns, which is approximately twice the time required for an electromagnetic wave to propagate from the first cavity to the last cavity.

The effects of the first-to-last time spread of drive pulses on the rise time and the duration time of output voltages are given in Fig. 16. The voltage rise time is nearly constant when t_{spread} is less than 25 ns. However, it increases sharping once the t_{spread} exceeds 30 ns. The voltage FWHM duration appears to increase linearly with t_{spread} when the two mistiming shots (shots 19-034 and 18-042) are excluded. For shot 18-042, the mistiming drive prolongs the rise time to approximately 52 ns, and then causes the diode impedance to collapse.

VII. SUMMARY AND FUTURE WORK

A four-stage IVA machine that generates high-brightness, small-focus-spot x rays for flash radiography has been manufactured and commissioned. A fully 3D electromagnetic model and circuit simulation was established and benchmarked against the electrical measurements. The simulated voltages downstream of each cavity agree well with the electrical measurements. The pulsed power performances and their fluctuations during the 54 successive shots were presented, including the peak output voltages, diode currents, x-ray durations, and radiated doses. The average peak output voltage is 4.4 ± 0.3 MV $(1-\sigma)$ and the average diode current is 81.6 ± 4.5 kA $(1-\sigma)$. Several typical failure modes originated from the diode-impedance collapse, insulator-stack-flashover, core saturation, and asynchronous drive were examined shot by shot. It was found that both the diode-impedance collapse and insulator-stack-flashover cause a sharp reduction in the x-ray duration time and the radiated doses, whereas the diode currents exhibit completely different characteristics. The former causes the diode current to increase well above the normal value, while the latter leads the diode current to decrease. During the 54 shots, the failure of the diode-impedance collapse occurs twice, and the insulator flashover occurs once.

The asynchronous drive affects the electrical pulses applied on the diode, and ultimately influences the radiation dose. The influences of the asynchronous drive on the output parameters (peak voltages, diode currents, rise time and duration time) are summarized from the statistics of almost 100 shots since the machine was commissioned. Both the peak output voltage and diode current gradually decreases as the first-to-last time spread of the four drive pulses became large.

In the future, the 3D EM model and circuit code will be further refined to better match the measured waveforms. Experiment tests associated with component reliability and output reproduction will continue. In addition, some experiments related to generation of double-pulse output will be attempted on the machine by local upgrades and modifications.

ACKNOWLEDGMENTS

The authors would like to thank Dr. Yixiang Hu, Professor Peitian Cong, Professor Wei Chen, Professor Wenyuan Liu, Professor Shuqing Ren, Professor Liangping Wang, Dr. Dingguo Lai, Dr. Qifu Xu, Dr. Mo Lee, and other colleagues in the team of Jianguang accelerator for their assistance. The work was supported by National Natural Science Foundation of China (Grant No. 11975186 and No. 51790524).

[1] C. Ekdahl, Modern electron accelerators for radiography, IEEE Trans. Plasma Sci. **30**, 254 (2002).

[2] T. J. Goldsack, T. F. Bryant, P. F. Beech, S. G. Clough, G. M. Cooper, R. Davitt, R. D. Edwards, N. Kenna, J. McLean, A. G. Pearce, M. J. Phillips, K. P. Pullinger, D. J. Short, M. A. Sinclair, K. J. Thomas, J. R. Threadgold, M. C. Williamson, and K. Krushelnick, Multimegavolt multiaxis high-resolution flash x-ray source development for a new hydrodynamics research facility at AWE aldermaston, IEEE Trans. Plasma Sci. **30**, 239 (2002).

[3] J. Maenchen, G. Cooperste, J. O' Malley, and I. Smith, Advances in pulsed power-driven radiography systems, Proc. IEEE **92**, 1021 (2004).

[4] J. J. Leckbee, J. E. Maenchen, D. L. Johnson, S. Portillo, D. M. VanDeVald, D. V. Rose, and B. V. Oliver, Design, simulation, and fault analysis of a 6.5-MV LTD for flash x-ray radiography, IEEE Trans. Plasma Sci. **34**, 1888 (2006).

[5] D. V. Rose, D. R. Welch, B. V. Oliver, J. J. Leckbee, J. E. Maenchen, D. L. Johnson, A. A. Kim, B. M. Kovalchuk, and V. A. Sinebryukhov, Numerical analysis of a pulsed compact LTD system for electron beam-driven radiography, IEEE Trans. Plasma Sci. **34**, 1879 (2006).

[6] M. Mazarakis, M. Cuneo, M. Hess, M. Kiefer, J. Leckbee, R. McKee, and D. Rovang, Multipulse electron diode development for flash radiography, in *Proceedings of the*

20th IEEE International Pulsed Power Conference, edited by M. Crawford and D. Wetz (IEEE, Piscataway, NJ, 2015), p. 569.

[7] M. G. Mazarakis, J. W. Poukey, J. E. Maenchen, D. C. Rovang, P. R. Menge, J. S. Lash, D. L. Smith, D. L. Johnson, J. A. Halbleib, S. R. Cordova, K. Mikkelson, J. Gustwiller, W. A. Stygar, D. R. Welch, I. Smith, and P. Corcoran, Inductive voltage adder (IVA) for submillimeter radius electron beam, in *Proceedings of the 11th IEEE International Pulsed Power Conference*, edited by G. Cooperstein and I. Vitkovitsky (IEEE, Piscataway, NJ, 1997), p. 642.

[8] B. V. Oliver, Recent advances in radiographic x-ray source development at Sandia, in *Proceedings of the 17th IEEE International High Power Particle Beams Conference, 2008*.

[9] J. M. Plewa, V. Bernigaud, T. Barnes, F. Poulet, A. Georges, R. Delaunay, M. Ribi'ere, C. Vermare, M. Yousfi, O. Eichwald, T. d 'Almeida, and R. Maisonny, High power electron diode for linear induction accelerator at a flash radiographic facility, Phys. Rev. Accel. Beams **21**, 070401 (2018).

[10] I. D. Smith, Induction voltage adders and the induction accelerator family, Phys. Rev. ST Accel. Beams **7**, 064801 (2004).

[11] I. Smith, P. Corcoran, V. Carboni, V. Bailey, H. Kishi, D. L. Johnson, J. Maenchen, I. Molina, R. Carlson, D. Fulton, K. Hahn, J. Smith, D. Droemer, K. Thomas, M. Phillips, S. Croxon, R. Forgan, and I. D. Smith, Induction voltage adder architectures and electrical characteristics, in *Proceedings of the 14th IEEE International Pulsed Power Conference*, edited by M. Giesselmann and A. Neuber (IEEE, Piscataway, NJ, 2003), p. 371.

[12] J. Maenchen, S. Cordova, J. Gustwiller, D. L. Johnson, P. Menge, I. Molina, C. Olson, S. Rosenthal, D. Rovang, B. Oliver, D. Welch, V. Bailey, I. Smith, D. Droemer, E. Hunt, G. MacLeod, and L. Woo, Inductive voltage adder driven x-ray sources for hydrodynamic radiography, in *Proceedings of the 12th IEEE International Pulsed Power Conference*, edited by C. Stallings and H. Kirbie (IEEE, Piscataway, NJ, 1999), p. 279.

[13] J. J. Ramirez, K. R. Prestwich, and I. D. Smith, High-power, short-pulse generators based on induction voltage adders, Proc. IEEE **80**, 946 (1992).

[14] J. E. Coleman, D. C. Moir, C. A. Ekdahl, J. B. Johnson, B. T. McCuistian, G. W. Sullivan, and M. T. Crawford, Increasing the intensity of an induction accelerator and reduction of the beam breakup instability, Phys. Rev. ST Accel. Beams **17**, 030101 (2014).

[15] R. D. Scarpetti, S. Nath, H. A. Davis, C. A. Ekdahl, S. A. Eversole, D. W. Jones, B. T. McCuistian, H. V. Smith, G. J. Caporaso, and S. S. Yu, Status of the DARHT 2nd axis at Los Alamos National Laboratory, in *Proceedings of the 15th IEEE International Pulsed Power Conference*, edited by J. Maenchen and E. Schamiloglu (IEEE, Piscataway, NJ, 2005), p. 37.

[16] V. Carboni, P. Corcoran, J. Douglas, I. Smith, D. Johnson, R. White, B. Altes, R. Stevens, H. Nishimoto, R. Carlson, J. Smith, P. Ortega, J. Chavez, J. Maenchen, E. Ormond, D. Nelson, D. Henderson, T. Helvin, V. Mitton, and B. Anderson, Pulse power performance of the Cygnus 1 and 2 radiographic sources, in *Proceedings of the 14th IEEE International Pulsed Power Conference*, edited by M. Giesselmann and A. Neuber (Ref. [11]), p. 905.

[17] D. Weidenheimer, P. Corcoran, R. Altes, J. Douglas, H. Nishimoto, I. Smith, R. Stevens, D. L. Johnson, R. White, J. Gustwiller, J. E. Maenchen, P. Menge, R. Carlson, R. D. Fulton, G. Cooperstein, D. Droemer, and E. Hunt, Design of a driver for the Cygnus x-ray source, in *Proceedings of the 13th IEEE International Pulsed Power Conference*, edited by B. Reinovsky and M. Newton (IEEE, Piscataway, NJ, 2001), p. 591.

[18] B. V. Oliver, Recent advances in radiographic x-ray source development at Sandia, in *17th International Conference on High Power Particle Beams (BEAMS), July, 2008* (IEEE, Piscataway, NJ, 2008), p. 1–5.

[19] T. Webb, M. Johnston, M. L. Kiefer, J. Leckbee, D. R. Welch, and N. Bennet, Evaluation of spot size and dose of the self-magnetic pinch diode on the RITS-6 accelerator from 3–8 MV, in *Proceedings of the 20th IEEE International Pulsed Power Conference*, edited by M. Crawford and D. Wetz (Ref. [6]), p. 1.

[20] I. Crotch *et al.*, Pulsed power driven flash x-ray sources for the hydrus project at AWE, in *Proceedings of the 16th IEEE International Pulsed Power Conference*, edited by E. Schamiloglu and F. Peterkin (IEEE, Piscataway, NJ, 2007), p. 1085.

[21] K. Thomas *et al.*, Status of the AWE hydrus IVA fabrication, in *Proceedings of the 18th IEEE International Pulsed Power Conference*, edited by R. D. Curry and B. V. Oliver (IEEE, Piscataway, NJ, 2011), p. 1042.

[22] W. P. Xie, The introduction of flash x-ray sources for radiography in institute of fluid physics, in *Proceedings of the 7th Europe-Asia Pulsed Power Conference and 22nd IEEE International High Power Particle Beams Conference* (unpublished).

[23] F. Guo, W. P. Xie, Z. Wang, J. H. Jiang, M. H. Xia, B. Wei, S. P. Feng, Y. Zhao, J. J. Kang, M. Wang, W. K. Zou, and L. Chen, Design of a 1-MV induction cavity and validation of the two-dimensional circuit model, Phys. Rev. Accel. Beams **22**, 020401 (2019).

[24] H. Wei, J. H. Yin, P. F. Zhang, F. J. Sun, A. C. Qiu, T. X. Liang, J. T. Zeng, X. F. Jiang, Z. G. Wang, J. Sun, W. Y. Liu, Q. F. Luo, W. D. Ding, and Y. X. Hu, Development of a 4-MV, 80-kA-induction voltage adder for flash x-ray radiography, IEEE Trans. Plasma Sci. **47**, 5030 (2019).

[25] D. Johnson, V. Bailey, R. Altes, P. Corcoran, I. Smith, S. Cordova, K. Hahn, J. Maenchen, I. Molina, S. Portillo, E. Puetz, M. Sceiford, D. Vandevalde, D. Rose, B. Oliver, D. Welch, and D. Droemer, Status of the 10 MV, 120 kA RITS-6 inductive voltage adder, in *Proceedings of the 15th IEEE International Pulsed Power Conference*, edited by J. Maenchen and E. Schamiloglu (Ref. [15]), p. 314.

[26] R. J. Commisso *et al.*, Status of the Mercury pulsed power generator, a 6-MV, 360-kA, magnetically-insulated inductive voltage adder, in *Proceedings of the 14th IEEE International Pulsed Power Conference*, edited by M. Giesselmann and A. Neuber (Ref. [11]), p. 383.

[27] J. P. Corley, J. A. Alexander, P. J. Pankuch, C. E. Heath, D. L. Johnson, J. J. Ramirez, and G. J. Denison, SABRE, a 10-MV linear induction accelerator, in *Proceedings of the 8th IEEE International Pulsed Power Conference*, edited by R. White and K. Prestwich (IEEE, Piscataway, NJ, 1991), p. 920.

[28] J. J. Ramirez, K. R. Prestwich, D. L. Johnson, J. P. Corley, G. J. Denison, J. A. Alexander, T. L. Franklin, P. J. Pankuch, T. W. L. Sanford, T. J. Sheridan, L. L. Torrison, and G. A. Zawadzkas, Performance of the Hermes-III gamma ray simulator, in *Proceedings of the 7th IEEE International Pulsed Power Conference*, edited by B. H. Bernstein and J. P. Shannon (IEEE, Piscataway, NJ, 1989), p. 26.

[29] J. H. Yin, F. J. Sun, A. C. Qiu, T. X. Liang, X. F. Jiang, T. F. Dang, J. T. Zeng, and Z. G. Wang, 2.8-MV low-inductance low-jitter electrical-triggered gas switch, IEEE Trans. Plasma Sci. **44**, 2045 (2016).

[30] B. V. Oliver *et al.*, Characterization of the rod-pinch diode x-ray source on Cygnus, in *Proceedings of the 17th IEEE International Pulsed Power Conference*, edited by B. H. Bernstein and J. P. Shannon (IEEE, Piscataway, NJ, 2009), p. 11.

[31] R. J. Commisso *et al.*, Overview of the 6-MV, rod-pinch experiment on Asterix, in *Proceedings of the 14th IEEE International Pulsed Power Conference*, edited by M. Giesselmann and A. Neuber (Ref. [11]), p. 479.

[32] F. C. Young *et al.*, Radiographic results for the rod-pinch diode scaled up to 6 MV, in *Proceedings of the 14th IEEE International Pulsed Power Conference*, edited by M. Giesselmann and A. Neuber (Ref. [11]), p. 979.

[33] F. Bayol, P. Charre, A Garrigues, C. Gonzales, F. Pompier, R. Vezinet, R. J. Commisso, F. C. Young, R. J. Allen, J. R. Boller, D. Mosher, S. B. Swanekamp, and G. Cooperstein, Evaluation of the rod-pinch diode as a high-resolution source for flash radiography at 2 to 4 MV, in *Proceedings of the 13th IEEE International Pulsed Power Conference*, edited by B. Reinovsky and M. Newton (Ref. [17]), p. 450.

[34] D. V. Rose, C. L. Miller, D. R. Welch, R. E. Clark, E. A. Madrid, C. B. Mostrom, W. A. Stygar, K. R. LeChien, M. A. Mazarakis, W. L. Langston, J. L. Porter, and J. R. Woodworth, Circuit models and three-dimensional electromagnetic simulations of a 1-MA linear transformer driver stage, Phys. Rev. ST Accel. Beams **13**, 090401 (2010).

[35] D. V. Rose, D. R. Welch, E. A. Madrid, C. L. Miller, R. E. Clark, W. A. Stygar, M. E. Savage, G. A. Rochau, J. E. Bailey, T. J. Nash, M. E. Sceiford, K. W. Struve, P. A. Corcoran, and B. A. Whitney, Three-dimensional electromagnetic model of the pulsed-power Z-pinch accelerator, Phys. Rev. ST Accel. Beams **13**, 010402 (2010).

[36] N. Bruner, T. Genoni, E. Madrid, D. Welch, K. Hahn, and B. Oliver, Excitation of voltage oscillations in an induction voltage adder, Phys. Rev. ST Accel. Beams **12**, 070401 (2009).

[37] R. Maisonny, M. Ribière, M. Toury, J. M. Plewa, M. Caron, and G. Auriel, and T. d'Almeida, Investigating the performances of a 1 MV high pulsed power linear transformer driver: from beam dynamics to x radiation, Phys. Rev. Accel. Beams **19**, 120401 (2016).

[38] H. Wei, F. J. Sun, A. C. Qiu, J. T. Zeng, J. H. Yin, T. X. Liang, and Y. X. Hu, Optimized design of azimuthal transmission lines for the cell driven by two PFLs in induction voltage adders, IEEE Trans. Plasma Sci. **41**, 2421 (2013).

[39] R. J. Allen, J. R. Boller, R. J. Commisso, F. C. Young, F. Bayol, P. Charre, and A. Garrigues, Adaptation of ASTERIX to positive polarity for 2 to 4-MV rod-pinch diode experiments and diode electrical analysis, in *Proceedings of the 13th IEEE International Pulsed Power Conference*, edited by B. Reinovsky and M. Newton (Ref. [17]), p. 446.

[40] E. M. Waisman, R. D. McBride, M. E. Cuneo, D. F. Wenger, W. E. Fowler, W. A. Johnson, L. I. Basilio, R. S. Coats, C. A. Jennings, D. B. Sinars, R. A. Vesey, B. Jones, D. J. Ampleford, R. W. Lemke, M. R. Martin, P. C. Schrafel, S. A. Lewis, J. K. Moore, M. E. Savage, and W. A. Stygar, Voltage measurements at the vacuum post-hole convolute of the Z pulsed-power accelerator, Phys. Rev. Accel. Beams **17**, 120401 (2014).

[41] F. C. Young, R. J. Commisso, R. J. Allen, D. Mosher, S. B. Swanekamp, G. Cooperstei, F. Bayol, P. Charre, A. Garrigues, C. Gonzales, F. Pompier, and R. Vezinet, Rod-pinch diode operation at 2 to 4 MV for high resolution pulsed radiography, Phys. Plasmas **9**, 4815 (2002).

[42] N. Bennett *et al.*, Shot reproducibility of the self-magnetic-pinch diode at 4.5 MV, Phys. Rev. Accel. Beams **17**, 050401 (2014).

[43] N. Bruner, D. R. Welch, K. D. Hahn, and B. V. Oliver, Anode plasma dynamics in the self-magnetic-pinch diode, Phys. Rev. ST Accel. Beams **14**, 024401 (2011).

[44] I. D. Smith, Flashover of vacuum interfaces with many stages and large transit times, IEEE Trans. Plasma Sci. **25**, 293 (1997).

[45] W. A. Stygar *et al.*, Operation of a five-stage 40,000-cm^2-area insulator stack at 158 kV/cm, in *Proceedings of the 12th IEEE International Pulsed Power Conference*, edited by C. Stallings and H. Kirbie (Ref. [12]), p. 454.

[46] W. A. Stygar *et al.*, Flashover of a vacuum-insulator interface: A statistical model, Phys. Rev. ST Accel. Beams **7**, 070401 (2004).

[47] C. W. Huddle, D. L. Johnson, G. J. Denison, and T. L. Franklin, Testing of the inductive cores for HERMES III, in *Proceedings of the 6th IEEE International Pulsed Power Conference*, edited by P. J. Turchi and B. H. Bernstein (IEEE, Piscataway, NJ, 1987), p. 494.

[48] A. A. Kim, M. G. Mazarakis, V. I. Manylov, V. A. Vizir, and W. A. Stygar, Energy loss due to eddy current in linear transformer driver cores, Phys. Rev. ST Accel. Beams **13**, 070401 (2010).

[49] R. Burdt and R. D. Curry, Magnetic core test stand for energy loss and permeability measurements at a high constant magnetization rate and test results for nanocrystalline and ferrite materials, Rev. Sci. Instrum. **79**, 094703 (2008).

[50] Y. X. Hu, J. T. Zeng, F. J. Sun, P. T. Cong, H. Wei, T. P. Sun, T. X. Liang, Z. F. Su, and A. C. Qiu, Effects of cell-driving jitters on the output voltage of magnetically

insulated induction voltage adders, IEEE Trans. Plasma Sci. **45**, 1004 (2017).

[51] J. D. Douglass *et al.*, 100 GW linear transformer driver cavity: design, simulations, and performance, Phys. Rev. Accel. Beams **21**, 120401 (2018).

[52] T. A. Holt, R. J. Allen, R. C. Fisher, R. J. Commisso, and D. L. Johnson, Analysis of switch performance on the Mercury pulsed-power generator, in *Proceedings of the 15th IEEE International Pulsed Power Conference*, edited by J. Maenchen and E. Schamiloglu (Ref. [15]), p. 128.

[53] P. Liu, F. J. Sun, H. Wei, Z. G. Wang, J. H. Yin, and A. C. Qiu, Influences of switching jitter on the operational performances of linear transformer drivers-based drivers, Plasma Sci. Technol. **14**, 347 (2012).